INORGANIC CHEMISTRY FRONTIERS

RESEARCH ARTICLE

View Article Online
View Journal | View Issue

Cite this: *Inorg. Chem. Front.*, 2022, **9**, 5853

Surface-halogen-introduced 2D NiCo bimetallic MOFs *via* a modulation method for elevated electrochemical glucose sensing†

Panpan Li,[a] Yang Bai,*[b,c] Guangxun Zhang,[a] Xiaotian Guo,[a] Xiangren Meng[d] and Huan Pang *[a]

Received 10th August 2022,
Accepted 18th September 2022

DOI: 10.1039/d2qi01738e

rsc.li/frontiers-inorganic

Two-dimensional (2D) metal–organic frameworks (MOFs) have been regarded as promising materials for electrochemical sensing, although plenty of efforts need to be devoted to enhancing their electrochemical performance. Herein, we have synthesized 2D NiCo bimetallic MOF nanoplates through a pyridine-modulated solvothermal synthesis and used 4-halogenpyridine for surface functionalization to overcome the shortcomings of the original MOFs. The 2D MOF nanoplates exhibit larger surface areas and higher densities of active sites than the cuboid structure. Besides, surface halogenation can improve the structural stability, generate more active sites, and enhance the interaction strength between MOFs and glucose (GLU). Specifically, the as-synthesized NiCoBP-Br exhibits excellent electrocatalytic performance for GLU with a quick response time of less than 2 s, and a high sensitivity of up to 1755.51 μA mM^{-1} cm^{-2} is achieved in the range of 0.5–6065.5 μM. This work will contribute to the evolution of MOF-based electrocatalysts and the improvement of their performance in electrochemical sensing.

Introduction

Metal–organic frameworks (MOFs) are an eminent class of highly porous, ordered crystalline materials built from organic ligands and metal clusters. Their large surface areas, diverse structures, and multiple functionalities have attracted considerable interest for chemical sensing, gas storage/separation, catalysis, batteries, and so on.[1–3] Compared with the conventional three-dimensional (3D) nanostructures, 2D MOFs have attracted extensive attention due to their advantages such as faster mass transport and more accessible active sites, which can promise more adequate contact with reactants and accelerate the reaction. These appealing features made them favorable candidates for improving performance in catalysis, electrocatalysis and sensing.[4–6]

The synthetic strategies of 2D MOF nanosheets can be divided into two categories: the top-down and the bottom-up methods.[7–11] The former means the exfoliation of layered nanostructured MOFs by breaking the weak interlayer interactions.[5,12–14] The latter involves direct synthesis with metal ions and organic ligands by selectively restricting the growth of MOFs along one direction and not affecting the other two directions, such as surfactant assisted synthesis, sonication synthesis, and modulated synthesis.[15,16] Modulated synthesis means the introduction of some small molecules such as acetic acid and pyridine which have similar functional groups to the original ligand and can compete to coordinate with metal clusters. They can selectively coordinate on crystal planes and inhabit the growth process of MOFs, resulting in anisotropic growth with different morphologies such as nanorods and nanosheets.[17–19] The atoms at the opposite side of the coordinating site of the modulator molecule could be exposed at the surface of MOFs. Accordingly, modulated synthesis is an effective and facile method to control the morphologies of MOFs and introduce surficial functional groups.

Accurate detection of GLU has attracted greater attention in clinical diagnostics, food industry, and biotechnology.[20] In the past few decades, various detection devices have been applied to detect GLU, such as electrical,[21] thermal,[22] and optical transducers.[23] Among these devices, the electrochemical method has drawn great attention, attributed to its easy operation process, excellent sensitivity, and low cost.[24] Electrochemical GLU sensors should have good selectivity, high sensitivity, and remarkable stability in electrochemical performance. MOFs have been considered one of the most promising materials in this field due to their large surface

[a]School of Chemistry and Chemical Engineering, Yangzhou University, Yangzhou, Jiangsu, 225009, China. E-mail: panghuan@yzu.edu.cn, huanpangchem@hotmail.com
[b]School of Pharmacy, Changzhou University, Changzhou, Jiangsu, 213164, P. R. China. E-mail: baiyang_nu@163.com
[c]State Key Laboratory of Coordination Chemistry, Nanjing University, Nanjing, Jiangsu, 210023, P. R. China
[d]School of Tourism and Cuisine, Yangzhou University, Yangzhou, 225127, China

†Electronic supplementary information (ESI) available. See DOI: https://doi.org/10.1039/d2qi01738e

areas, rich metal ion centers and diverse structures.[25] However, MOFs still have several shortcomings such as weak chemical stability when they come into contact with water, less active sites on the surface, and minor interaction strength with GLU, which seriously affect their practical applications.[26,27] To address these shortcomings, rational modification strategies for MOFs should be proposed.[28,29]

Halogenated molecules show special properties such as low surface tension and surface free energy due to the high electronegativity and polarizability of halogens.[29–31] Pang *et al.* reported that MOFs constructed using halogenated organic ligands showed improved chemical stability.[30] Moreover, halogenation is also an effective strategy to tune or improve the functionalities of MOF materials.[32] Adding polar functional groups on the surface of MOFs has been proved to be an effective method to strengthen the interaction between MOFs and the guest species.[28,33–36] Besides, polar functional groups, such as hydroxyl-, amino-, carboxyl-, and nitro-groups, and halogens, can influence the charge distribution of adjacent atoms through their higher electronegativity,[36,37] thereby generating more active sites and enhancing the GLU oxidation reaction (GOR).[38]

Halogenated MOFs obtained by directly introducing pre-functionalized ligands have rarely been reported. Meek *et al.* reported a series of halogenated MOF-5 which use halogenated terephthalic acid as the ligand and $Zn(NO_3)_2{\cdot}6H_2O$ as the metal source.[39] Cohen *et al.* reported a series of halogenated derivatives of UiO-66 using halogenated terephthalic acid as the starting ligand.[40] However, those methods were decorating halogen on the inner surface of MOFs. There is a lack of an effective method to introduce halogen on the surface of MOFs through covalent bonds which would improve the electrochemical function.

Herein, we report a facile synthesis of NiCo bimetallic MOF nanoplates *via* a one-pot method by introducing pyridine as a modulator. Simultaneously, 4-bromopyridine or 4-iodopyridine was also introduced to improve the chemical stability, generate more active sites, and increase the interaction between the MOFs and GLU. Among the 2D NiCo-MOF nanoplates, NiCoBP-Br displayed the best GOR sensing activity, showing a quick response time of less than 2 s and achieving a sensitivity of 1755.51 μA mM^{-1} cm^{-2} with a wide linear response of 0.5–6065.5 μM. Moreover, the response current remained 99.5% after cycling for 6000 s. Tests on NiCoBP-Br after cycling for 12 hours showed that the sources of high electrocatalytic activity were hydroxides and the oxyhydroxide species formed during the reaction within the inherited 2D morphology.

Results and discussion

The 2D MOFs were synthesized as shown in Scheme 1. First, 4,4′-bipyridine, $NiSO_4{\cdot}6H_2O$ and $CoSO_4{\cdot}7H_2O$ were dissolved in water. Next, 4-bromopyridine or 4-iodopyridine was dissolved in EtOH containing pyridine. Then the mixture was added to the previous solution and heated at 100 °C for 24 h to acquire

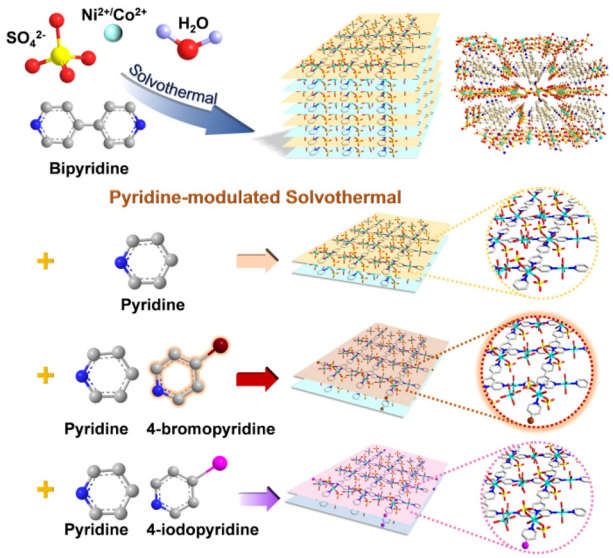

Scheme 1 Schematic illustration of the synthetic strategy of the cuboid NiCo-B MOFs and the NiCo-BP, NiCoBP-Br, and NiCoBP-I nanoplates.

the 2D MOFs. The specific molar concentrations and synthesis procedures are provided in the Experimental section.

The morphology of the 2D MOFs was analyzed by scanning electron microscopy (SEM) (Fig. 1a_1–c_1). They all have uniform

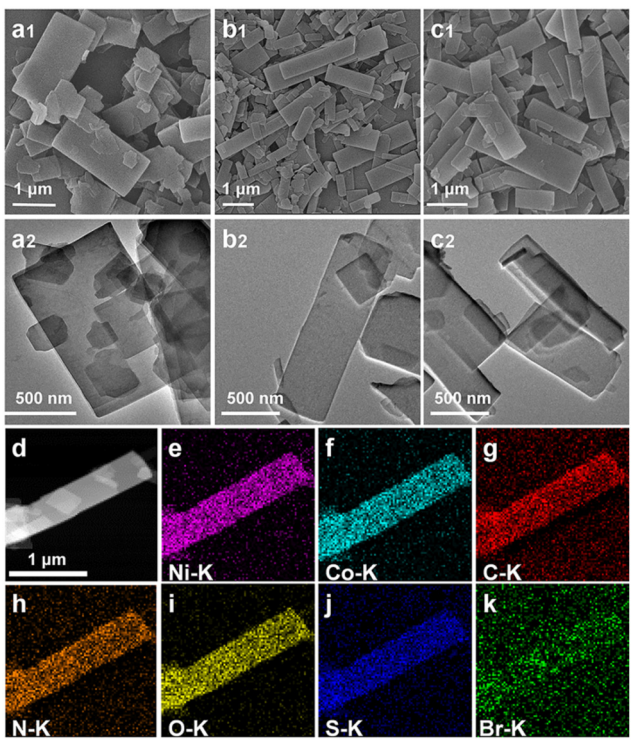

Fig. 1 Morphological characterization of 2D NiCo-MOFs. SEM images of (a_1) NiCoBP, (b_1) NiCoBP-Br, and (c_1) NiCoBP-I; TEM images of (a_2) NiCoBP, (b_2) NiCoBP-Br, and (c_2) NiCoBP-I; (d–k) HAADF-STEM and elemental mappings of (e) Ni–K, (f) Co–K, (g) C–K, (h) N–K, (i) O–K, (j) S–K, and (k) Br–K in NiCoBP-Br.

scales, well-defined morphologies, and smooth surfaces. NiCoBP-Br obtained after the introduction of 4-bromopyridine exhibited a longer longitudinal dimension than NiCoBP. On the other hand, NiCoBP-I obtained after the introduction of 4-iodopyridine exhibited a more uniform and regular morphology. The transmission electron microscopy (TEM) images agreed well with the SEM results (Fig. 1a$_2$–c$_2$). 4,4′-Bipyridine is a bidentate ligand that can link metal ions and contribute to the formation of MOFs in all dimensions. Pyridine is a monodentate ligand and just half of 4,4′-bipyridine which can link metal ions and inhibit the growth of MOFs in a vertical direction to form the 2D structure. To demonstrate the modulating function of pyridine, NiCoB was synthesized in the absence of pyridine (Fig. S1a and b†), and the distinct difference between the 2D structure and the cuboid MOF demonstrates the restricted ability of pyridine. Besides, due to the selective coordination of pyridine in the vertical direction, halogens mainly exist on the surface of the 2D structures (Scheme 1). The surface functionalization can enhance the hydrophobicity and stability of the structure, improve the affinity with the reactant molecules, and produce more active sites. According to the nitrogen adsorption/desorption isotherms, NiCoBP (40.357 m^2 g^{-1}) shows a higher specific surface area (SBET) than NiCoB (3.896 m^2 g^{-1}), benefitting from its unique 2D structure (Fig. S2a–d†).

X-ray diffraction (XRD) was used to study the crystallographic structure and phase purity. As shown in Fig. 2a, NiCoB possessed a good crystal structure, which was in great agreement with that of Co MOFs (MOFs ([Co_3(4,4′-bpy)$_2$(SO_4)$_3$(H_2O)$_{11}$]$_n$, Cambridge Crystallographic Data Centre (CCDC 826371)), as reported in the previous literature.[41] With the addition of pyridine, 4-bromopyridine, and 4-iodopyridine, the diffraction peaks at 16.8° (020), 17.8° (112), 18.2° (102), 23.5° (102), and 25.5° (200) match well with those of the reported Co MOFs, meaning that they retained their original structure. At the same time, new diffraction peaks of NiCoBP-Br and NiCoBP-I began to appear (at 6.6°, 9.7°and 11.6°), revealing the successful coordination of the new ligands. We further studied the FT-IR spectra of these NiCo-MOF materials, and as shown in Fig. 2b, the results showed that the functional groups were retained after the addition of pyridine, 4-bromopyridine and 4-iodopyridine. The absorbed peaks at 1614, 1534, 1488 and 1408 cm^{-1} were the vibration absorption peaks of the pyridine skeleton (Fig. 2b gray area). Furthermore, the absorption peaks at 1089 and 619 cm^{-1} demonstrated the presence of the SO_4^{2-} ions (Fig. 2b yellow area).

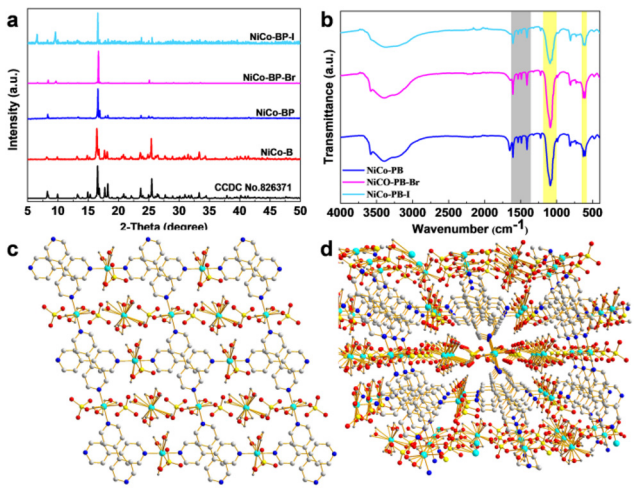

Fig. 2 The XRD patterns, FTIR spectra and crystal structures of the NiCo-MOFs. (a) Powder XRD patterns of the NiCo-MOFs. (b) FTIR spectra of the NiCo-MOFs. (c and d) Structural schematic graphs of Co-bpy [Co_3(4,4′-bpy)$_2$(SO_4)$_3$(H_2O)$_{11}$]$_n$. (c) Crystal stacking along the a axis. (d) Crystal stacking along the c axis.

X-ray photoelectron spectroscopy (XPS) was used to acquire the chemical structure and surficial electronic state information of the NiCo-MOF samples. According to the survey spectra, all the samples with pyridine contained Ni, Co, C, N, O, and S (Fig. S5a–c†). Moreover, the presence of elements Br and I in NiCoBP-Br and NiCOBP-I respectively demonstrated the successful coordination of 4-halogenpyridine (Fig. 1k, Fig. S3h, S5b and c†), which is consistent with the elemental mapping results. Taking NiCo-BP-Br as an example, in the high-resolution spectra of Co 2p, the peaks at 797.4 and 781.5 eV corresponded to Co^{2+} 2p$_{1/2}$ and 2p$_{3/2}$, respectively (Fig. 3a). Furthermore, the peaks at 856.1 and 873.7 eV could be referred to Ni^{2+} 2p$_{3/2}$ and Ni^{2+} 2p$_{1/2}$, respectively (Fig. 3b).[42–44] The C 1s XPS profile had two distinct peaks at 285.2 and 286.1 eV, which corresponded to the C–N and C–C bonds from the 4-halogenpyridine, pyridine or 4,4′-bipyridine ligands (Fig. 3c).[44] In the XPS spectrum of N 1s, the peak was deconvoluted into two main peaks located at 399.8 and 401.4 eV, which corresponded to pyrrolic N and pyridinic N, respectively (Fig. 3d).[45] The presence of 4-bromopyridine in NiCoBP-Br was confirmed through the 3d peaks of Br at 68.8 (3d$_{3/2}$) and 70.1 (3d$_{5/2}$) eV (Fig. 3e). The presence of 4-iodopyridine in NiCoBP-I was confirmed through the I 3d peaks at 631.2 (3d$_{3/2}$) and 619.7 (3d$_{5/2}$) eV (Fig. 3f).[28,38] All these results indicated the existence of the C–X bond and the successful coordination of the 4-halogenpyridine.

To evaluate the electrochemical performance of the synthesized MOFs for the GOR, a series of electrochemical measurements were implemented using a three-electrode configuration in a 0.1 mol L^{-1} NaOH solution. The electrocatalytic performances of NiCoBP, NiCoBP-Br, and NiCoBP-I GCE are shown in Fig. 4. Cyclic voltammetry (CV) is a reliable method to investigate the electrochemical oxidation and reduction process of GLU. The increasing current with the addition of GLU demonstrates that NiCoBP-Br GCE can catalyze the oxidation and reduction process of GLU over a large concentration range (Fig. 4a). The NiCoBP and NiCoBP-I electrodes showed similar curves, demonstrating that they can also catalyze GLU (Fig. S7 and S8†). The oxidation currents of NiCoBP, NiCoBP-Br and NiCoBP-I GCE were tested in the NaOH solution (0.1 M) with 10 μM GLU at a scan rate of 5 mV s^{-1}. The magnitude of the oxidation current is NiCoBP-Br > NiCoBP-I >

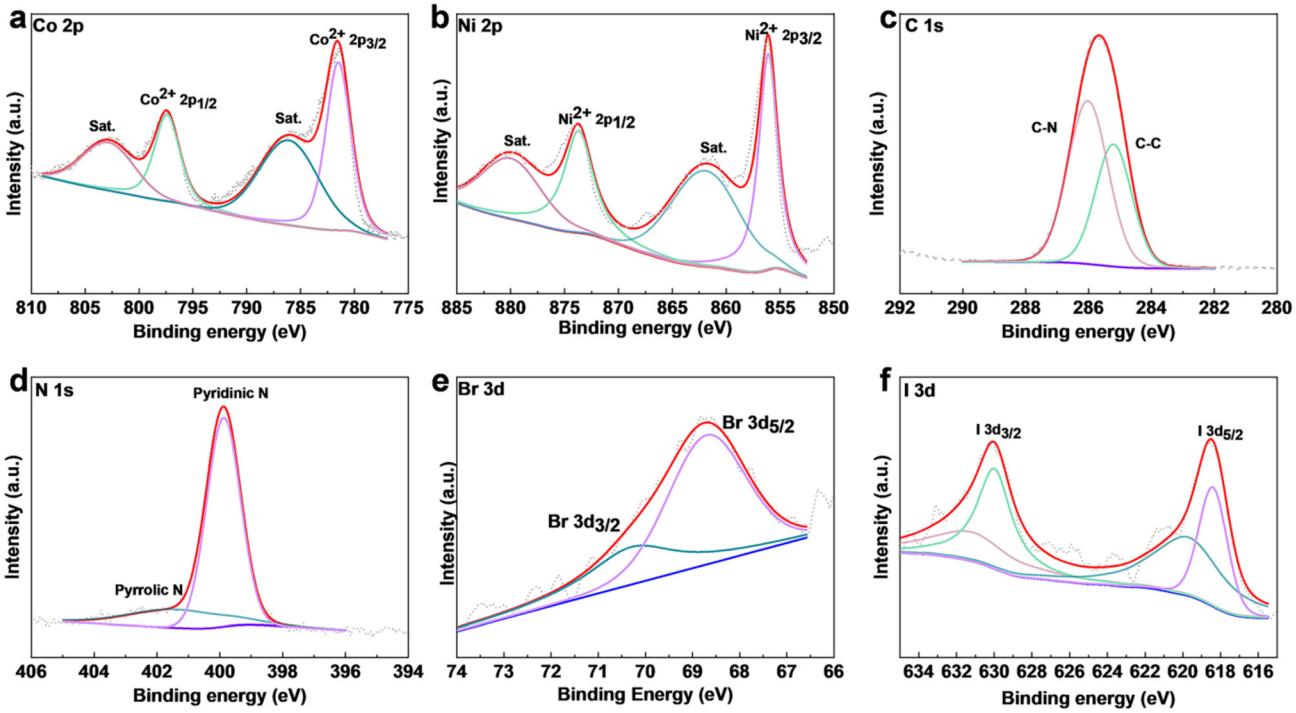

Fig. 3 XPS of NiCoBP-Br and NiCoBP-I. (a–e) High-resolution (a) Co 2p, (b) Ni 2p, (c) C 1s, (d) N 1s, and (e) Br 3d XPS spectra of NiCoBP-Br. (f) High-resolution I 3d XPS spectra of NiCoBP-I.

NiCoBP GCE, indicating that the NiCoBP-Br GCE has the most excellent electrocatalytic ability among the three materials (Fig. 4d). At the same time, the appearance of redox peaks in the range of 0.25–0.6 V could be attributed to the redox reactions of the nickel and cobalt-based composites. The proposed electrocatalytic mechanisms are as follows (Scheme 1):

$$\mathrm{Co(II)Ni(II)\text{-}MOFs} \rightarrow \mathrm{Co(III)Ni(III)\text{-}MOFs} + 2e^-$$

$$\mathrm{Co(III)Ni(III)\text{-}MOFs} + 2OH^- + 2GLU \rightarrow$$

$$\mathrm{Co(II)Ni(II)\text{-}MOFs} + 2\mathrm{Glucolactone} + 2H_2O + 2e^-$$

The amperometric technique is a reliable method to evaluate the electrochemical activity and study the basic electrochemical parameters of the modified electrodes. In order to acquire the optimum amperometric signal, the applied potentials from 0.4 to 0.55 V were tested for the modified electrodes with a stepwise addition of GLU (1.0×10^{-3} M) (Fig. 4b, S9 and S10†). In the NiCoBP-Br GCE, the current increment was enhanced with the working potential being increased until it reached 0.55 V. Therefore, 0.55 V was chosen as the testing potential in the following experiments.

Fig. 4e and Fig. S6a† show the current–time plot of the NiCoBP-Br GCE with the addition of GLU in 0.1 M NaOH at 0.55 V. The oxidation currents increased with the successive addition of GLU and reached the maximum steady-state in less than 2 s (Fig. S6b†). This demonstrates that the NiCoBP-Br GCE performed well in the mass adsorption/diffusion and electron-exchange process, which are necessary for constructing sensors. Fig. S6a† shows the magnification of the current of NiCoBP-Br induced by a low concentration of GLU after the initial current is stable. Even a low concentration of 0.5 μM can cause a current response which proves the excellent electrocatalytic sensitivity of the material. Moreover, the NiCoBP-Br GCE exhibited a linear relationship between current responses and the GLU concentrations from 0.5 to 6065.5 μM, whose linear regression equation was $I(\mu A) = 21.19298 + 0.12409C$ (μM), $R^2 = 0.99667$, and the sensitivity was about 1755.51 μA mM^{-1} cm^{-2}. The detection limit was as low as 0.0665 μM with an S/N ratio of 3 (Fig. S6c†). The NiCoBP GCE and the NiCoBP-I GCE show similar sensing behavior (Fig. S11c and S12c†). Upon comparison, the NiCoBP GCE showed the widest linear range and the NiCoBP-Br GCE showed the highest sensitivity and the lowest detection limit (Fig. 4e and f).

Moreover, selectivity is a major parameter in sensing testing. As shown in Fig. S6d,† the NiCoBP-Br GCE has an obvious current response of GLU, whereas a minimal current response was observed when interferents such as ascorbic acid (AA, 5 μM), dopamine (DA, 5 μM), uric acid (UA, 5 μM), and NaCl (5 μM) were added, which demonstrates that the NiCoBP-Br GCE possessed excellent selectivity against interfering species in blood. The same test on the NiCoBP and NiCoBP-I GCEs showed similar anti-interference performance (Fig. S13 and S16†). Upon comparison, the NiCoBP-Br GCE showed a higher sensitivity for GLU (Fig. 4g). Accordingly, it possesses the best selectivity performance and highest sensitivity among the three electrodes (Fig. 4g).

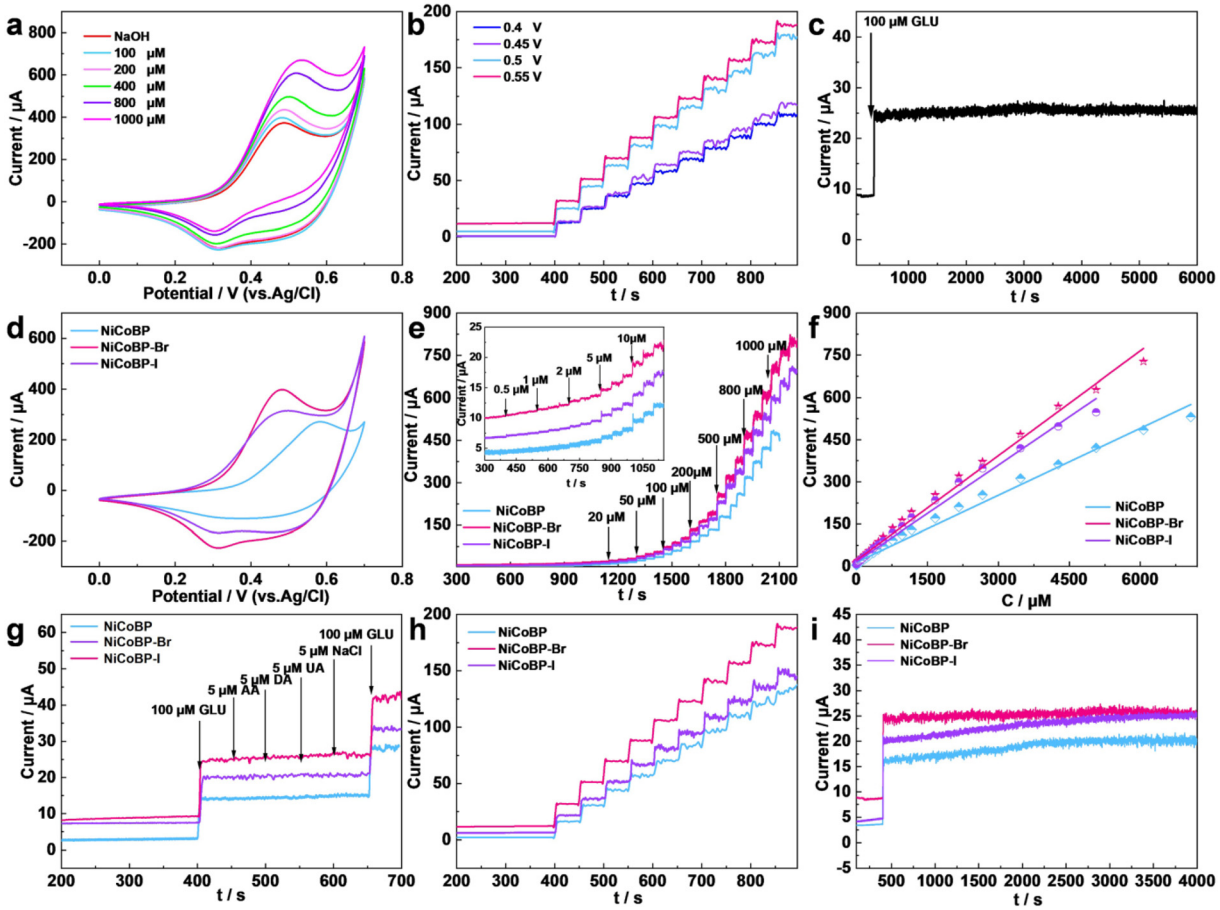

Fig. 4 Electrochemical performances of the 2D NiCo-MOF GCE: (a–c) NiCoBP-Br GCE. (a) CV curves in NaOH (0.1 M) when adding different concentrations of GLU. (b) Amperometric responses of the NiCoBP-Br GCE at different potentials (from 0.40 to 0.55 V) with continuous addition of 100 μM GLU in 0.1 M NaOH. (c) The stability of the response current for the NiCoBP-Br GCE after the addition of GLU solution (100 μM) over 6000 s. (d–i) NiCoBP, NiCoBP-Br, and NiCoBP-I GCE. (d) CV curves of the NiCoBP, NiCoBP-Br, NiCoBP-I GCE in NaOH (0.1 M) with 10 μM GLU. (e) Current–time response of the NiCoBP, NiCoBP-Br, and NiCoBP-I GCE at 0.55 V on successive additions of different amounts of GLU in 0.1 M NaOH. (f) A plot of electrocatalytic current of GLU *vs.* its concentrations in the range of 0.5 μM to 6.065 mM. (g) Current–time responses of the NiCoBP, NiCoBP-Br, and NiCoBP-I GCE with the addition of 100 μM GLU, 5 μM AA, 5 μM DA, 5 μM UA, 5 μM NaCl, and 100 μM GLU into 0.1 M NaOH at 0.55 V. (h) Current–time response of the NiCoBP, NiCoBP-Br, and NiCoBP-I GCE with the continuous addition of 100 μM GLU at 0.55 V. (i) The stability of the response current for the NiCoBP, NiCoBP-Br, and NiCoBP-I GCE after the addition of GLU solution (100 μM) over 4000 s.

To avoid experimental errors caused by coincidences, repeatability and stability of the MOFs were tested. As shown in Fig. 4h, the repeatability of the MOF GCE was measured to detect 100 μM GLU ten times. The detected relative standard deviation (RSD) of the NiCoBP-Br GCE was 2.63%, exhibiting a high repeatability. At the same time, the NiCoBP and NiCoBP-I GCEs also have good repeatability and the NiCoBP-Br GCE exhibited the largest current response. As shown in Fig. 4c, the curve demonstrates the stability of the NiCoBP-Br GCE in the presence of 100 μM GLU in 0.1 M NaOH solution over 6000 s. The result shows that there is only 0.118% current loss after 6000 s. At the same time, the NiCoBP and NiCoBP-I GCEs show almost no loss after 4000 s (Fig. 4i, S14 and S17†).

To further investigate the GOR mechanism of the MOF materials, the morphology, structure, and chemical variation after the GOR were obtained. The SEM and TEM images show that the morphology of NiCoBP-Br was maintained after cycling for 12 h, with smaller sizes and thickness which contribute to more active sites. The HRTEM image shows obvious lattice fringes and the interplanar distances were about 0.24, 0.28, and 0.27 nm, corresponding to the (021) plane of CoO(OH) (JCPDS No. 26-0480), the (100) plane of $Co(OH)_2$ (JCPDS No 74-1057) and the (100) plane of $Ni(OH)_2$ (JCPDS No 14-0117) (Fig. 5c). In Fig. 5d, several bright rings with discrete spots could be seen according to the selective area electron diffraction (SAED) pattern, which could be indexed to the (130)/(221) planes of CoO(OH), the (101)/(210) planes of NiO(OH) (JCPDS No. 27-0956), and the (113) plane of $Co(OH)_2$. In addition, the elemental mapping images of NiCoBP-Br after cycling show that Ni, Co, C, N, O, S and Br were dispersed uniformly throughout the nanoplate (Fig. 5e–l). It indicates that these elements have been preserved although there was a structural variation after the GOR test. The XRD patterns indicated that NiCoBP-Br after cycling showed good crystallinity

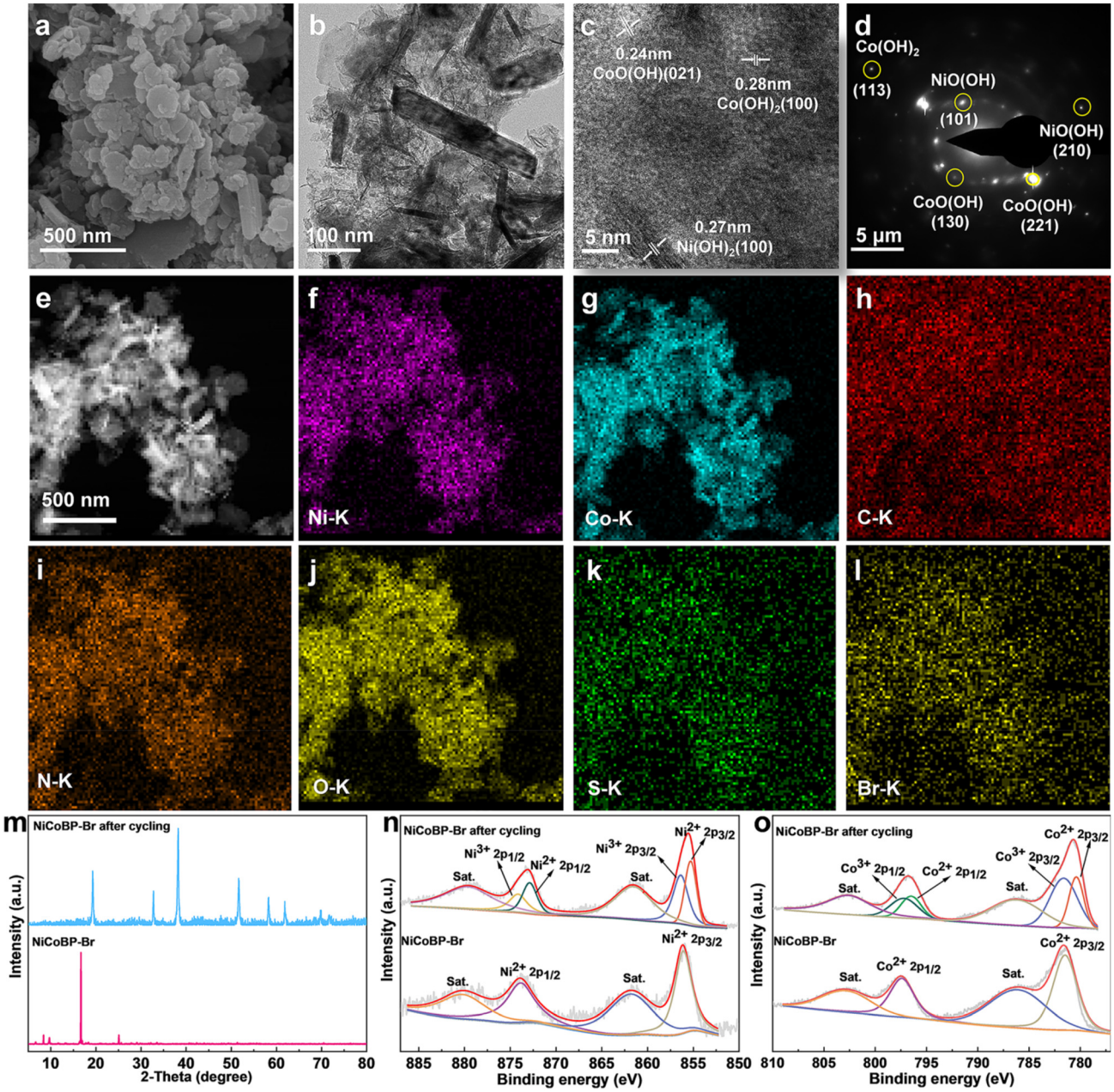

Fig. 5 Structural characterization of NiCoBP-Br after cycling. (a) SEM, (b)TEM, and (c) HRTEM images and (d) SAED pattern of NiCoBP-Br after cycling for 12 h. (e–l) HAADF-STEM and elemental mappings of (f) Ni–K, (g) Co–K, (h) C–K, (i) N–K, (j) O–K, (k) S–K, and (l) Br–K in NiCoBP-Br after cycling for 12 h. (m) XRD patterns of NiCoBP-Br after cycling for 12 h. (n and o) High-resolution XPS spectra of (n) Ni 2p and (o) Co 2p of NiCoBP-Br before (bottom) and after (top) cycling for 12 h.

and all peaks can be pointed to $Co(OH)_2/Ni(OH)_2$, which is agreed with the HRTEM image. Moreover, the XPS spectra were analyzed to detect the changes in the chemical states. The Ni 2p spectra showed that the Ni^{2+} $2p_{1/2}$ and Ni^{2+} $2p_{3/2}$ peaks moved to a lower binding energy after cycling (Ni^{2+} $2p_{3/2}$ from 856.1 to 855.2 eV and Ni^{2+} $2p_{1/2}$ from 873.7 to 872.8 eV). It may be due to the destruction of the Ni–N bonds and the formation of the Ni–O bonds directly which can increase the electron density and develop a lower binding energy of Ni 2p in $Ni(OH)_2$.[46] At the same time, two new peaks at 874.2 and 856.5 eV appeared which demonstrates the presence of Ni^{3+} in the formed NiO(OH). The high-resolution spectra of Co exhibit a similar phenomenon, the lower-shifted Co^{2+} 2p peaks (Co^{2+} $2p_{1/2}$ from 797.4 to 796.5 eV and Co^{2+} $2p_{3/2}$ from 781.5 to 780.4 eV) and the appearance of two new Co^{3+} peaks (781.03 and 797.2 eV) showed the possible structural variation from NiCoBP-Br to $Co(OH)_2$ and CoO(OH). Therefore, the enhanced GOR activity of NiCoBP-Br could be ascribed to the generated active hydroxide and oxyhydroxide species. The function of surface halogenation can be summarized as follows: first, it

improves the structural stability of 2D NiCo-MOFs in water. Second, it can influence the charge distribution of adjacent atoms through their higher electronegativity, thereby generating more active sites and enhancing the GOR. Third, it could also enhance the interaction strength between the MOFs and GLU to increase the reaction rate.

Conclusion

In summary, NiCo bimetallic MOF nanoplates were obtained using a facile method through the introduction of pyridine as a modulator. Introducing polar halogen molecules on the surface of MOFs has been proved to be an effective method to improve GOR performances of the as-prepared MOF materials. Among the halogenated NiCo-MOF nanoplates, NiCoBP-Br showed the best GOR sensing activity. A sensitivity of up to 1755.51 μA mM^{-1} cm^{-2} is achieved with a wide linear response of 0.5–6065.5 μM and a quick response time of less than 2 s. Moreover, nearly no loss of the response current was observed after cycling for 6000 s. Investigation of NiCoBP-Br after cycling for 12 h showed that the sources of high electrocatalytic activity were hydroxides and the oxyhydroxide species formed during the reaction with the inherited 2D morphology. We expect that this work will facilitate the evolution of MOF-based electrocatalysts and improve their performance in electrochemical sensing applications.

Conflicts of interest

There are no conflicts to declare.

Acknowledgements

This work was supported by the National Natural Science Foundation of China (U1904215), the Natural Science Foundation of Jiangsu Province (BK20200044), and the Changjiang Scholars Program of the Ministry of Education (Q2018270). The authors acknowledge the Priority Academic Program Development of Jiangsu Higher Education Institutions.

References

1 H. Furukawa, K. E. Cordova, M. O'Keeffe and O. M. Yaghi, The chemistry and applications of metal-organic frameworks, *Science*, 2013, **341**, 1230444.
2 G. Lee, S. Lee, S. Oh, D. Kim and M. Oh, Tip-To-Middle Anisotropic MOF-On-MOF Growth with a Structural Adjustment, *J. Am. Chem. Soc.*, 2020, **142**, 3042–3049.
3 D. B. Gorle, S. Ponnada, M. S. Kiai, K. K. Nair, A. Nowduri, H. C. Swart, E. H. Ang and K. K. Nanda, Review on recent progress in metal-organic framework-based materials for fabricating electrochemical glucose sensors, *J. Mater. Chem. B*, 2021, **9**, 7927–7954.
4 J. Wang, N. Li, Y. X. Xu and H. Pang, Two-Dimensional MOF and COF Nanosheets: Synthesis and Applications in Electrochemistry, *Chem. – Eur. J.*, 2020, **26**, 6402–6422.
5 M. T. Zhao, Y. Huang, Y. W. Peng, Z. Q. Huang, Q. L. Ma and H. Zhang, Two-dimensional metal-organic framework nanosheets: synthesis and applications, *Chem. Soc. Rev.*, 2018, **47**, 6267–6295.
6 Y. Bai, C. L. Liu, T. T. Chen, W. T. Li, S. S. Zheng, Y. C. Pi, Y. S. Luo and H. Pang, MXene-Copper/Cobalt Hybrids via Lewis Acidic Molten Salts Etching for High Performance Symmetric Supercapacitors, *Angew. Chem., Int. Ed.*, 2021, **60**, 25318–25322.
7 J. N. Coleman, M. Lotya, A. O'Neill, S. D. Bergin, P. J. King, U. Khan, K. Young, A. Gaucher, S. De, R. J. Smith, I. V. Shvets, S. K. Arora, G. Stanton, H. Y. Kim, K. Lee, G. T. Kim, G. S. Duesberg, T. Hallam, J. J. Boland, J. J. Wang, J. F. Donegan, J. C. Grunlan, G. Moriarty, A. Shmeliov, R. J. Nicholls, J. M. Perkins, E. M. Grieveson, K. Theuwissen, D. W. McComb, P. D. Nellist and V. Nicolosi, Two-dimensional nanosheets produced by liquid exfoliation of layered materials, *Science*, 2011, **331**, 568–571.
8 F. Song and X. L. Hu, Exfoliation of layered double hydroxides for enhanced oxygen evolution catalysis, *Nat. Commun.*, 2014, **5**, 4477.
9 P. Q. Liao, N. Y. Huang, W. X. Zhang, J. P. Zhang and X. M. Chen, Controlling guest conformation for efficient purification of butadiene, *Science*, 2017, **356**, 1193–1196.
10 S. Wang, C. M. McGuirk, A. d'Aquino, J. A. Mason and C. A. Mirkin, Metal-Organic Framework Nanoparticles, *Adv. Mater.*, 2018, **30**, 1800202.
11 Q. Wang and D. Astruc, State of the Art and Prospects in Metal-Organic Framework (MOF)-Based and MOF-Derived Nanocatalysis, *Chem. Rev.*, 2020, **120**, 1438–1511.
12 X. L. Wang, H. Xiao, A. Li, Z. Li, S. J. Liu, Q. H. Zhang, Y. Gong, L. R. Zheng, Y. Q. Zhu, C. Chen, D. S. Wang, Q. Peng, L. Gu, X. D. Han, J. Li and Y. D. Li, Constructing NiCo/Fe3O4 Heteroparticles within MOF-74 for Efficient Oxygen Evolution Reactions, *J. Am. Chem. Soc.*, 2018, **140**, 15336–15341.
13 Y. Bai, G. X. Zhang, S. S. Zheng, Q. Li, H. Pang and Q. Xu, Pyridine-modulated Ni/Co bimetallic metal-organic framework nanoplates for electrocatalytic oxygen evolution, *Sci. China Mater.*, 2021, **64**, 137–148.
14 L. Lin, Q. Zhang, Y. Ni, L. Shang, X. Zhang, Z. Yan, Q. Zhao and J. Chen, Rational design and synthesis of two-dimensional conjugated metal-organic polymers for electrocatalysis applications, *Chem*, 2022, **8**, 1822–1854.
15 L. Y. Cao, Z. K. Lin, F. Peng, W. W. Wang, R. Y. Huang, C. Wang, J. W. Yan, J. Liang, Z. M. Zhang, T. Zhang, L. S. Long, J. L. Sun and W. B. Lin, Self-Supporting Metal-Organic Layers as Single-Site Solid Catalysts, *Angew. Chem., Int. Ed.*, 2016, **55**, 4962–4966.
16 Y. L. Liu, X. Y. Liu, L. Feng, L. X. Shao, S. J. Li, J. Tang, H. Cheng, Z. Chen, R. Huang, H. C. Xu and J. L. Zhuang, Two-Dimensional Metal-Organic Framework Nanosheets:

Synthesis and Applications in Electrocatalysis and Photocatalysis, *ChemSusChem*, 2022, **15**, e202102603.

17 Y. Sakata, S. Furukawa, M. Kondo, K. Hirai, N. Horike, Y. Takashima, H. Uehara, N. Louvain, M. Meilikhov, T. Tsuruoka, S. Isoda, W. Kosaka, O. Sakata and S. Kitagawa, Shape-Memory Nanopores Induced in Coordination Frameworks by Crystal Downsizing, *Science*, 2013, **339**, 193–196.

18 C. Y. Li, J. Wang, Y. Yan, P. W. Huo and X. K. Wang, MOF-derived NiZnCo-P nano-array for asymmetric supercapacitor, *Chem. Eng. J.*, 2022, **446**, 8.

19 K. B. Wang, Q. Xun and Q. C. Zhang, Recent progress in metal-organic frameworks as active materials for supercapacitors, *EnergyChem*, 2020, **2**, 32.

20 M. Adeel, K. Asif, M. M. Rahman, S. Daniele, V. Canzonieri and F. Rizzolio, Glucose Detection Devices and Methods Based on Metal–Organic Frameworks and Related Materials, *Adv. Funct. Mater.*, 2021, **31**, 2106023.

21 A. J. Bandodkar, S. Imani, R. Nunez-Flores, R. Kumar, C. Y. Wang, A. M. V. Mohan, J. Wang and P. P. Mercier, Reusable electrochemical glucose sensors integrated into a smartphone platform, *Biosens. Bioelectron.*, 2018, **101**, 181–187.

22 C. D. Malchoff, K. Shoukri, J. I. Landau and J. M. Buchert, A novel noninvasive blood glucose monitor, *Diabetes Care*, 2002, **25**, 2268–2275.

23 M. S. Steiner, A. Duerkop and O. S. Wolfbeis, Optical methods for sensing glucose, *Chem. Soc. Rev.*, 2011, **40**, 4805–4839.

24 Q. Jing, W. Li, J. Wang, X. Chen and H. Pang, Calcination activation of three-dimensional cobalt organic phosphate nanoflake assemblies for supercapacitors, *Inorg. Chem. Front.*, 2021, **8**, 4222–4229.

25 Y. Peng, J. Xu, J. Xu, J. Ma, Y. Bai, S. Cao, S. Zhang and H. Pang, Metal-organic framework (MOF) composites as promising materials for energy storage applications, *Adv. Colloid Interface Sci.*, 2022, **307**, 102732.

26 L. Wang, X. Feng, L. T. Ren, Q. H. Piao, J. Q. Zhong, Y. B. Wang, H. W. Li, Y. F. Chen and B. Wang, Flexible Solid-State Supercapacitor Based on a Metal-Organic Framework Interwoven by Electrochemically-Deposited PANI, *J. Am. Chem. Soc.*, 2015, **137**, 4920–4923.

27 X. F. Lu, P. Q. Liao, J. W. Wang, J. X. Wu, X. W. Chen, C. T. He, J. P. Zhang, G. R. Li and X. M. Chen, An Alkaline-Stable, Metal Hydroxide Mimicking Metal-Organic Framework for Efficient Electrocatalytic Oxygen Evolution, *J. Am. Chem. Soc.*, 2016, **138**, 8336–8339.

28 T. M. M. Ntep, H. Breitzke, L. Schmolke, C. Schlusener, B. Moll, S. Millan, N. Tannert, I. El Aita, G. Buntkowsky and C. Janiak, Facile in Situ Halogen Functionalization via Triple-Bond Hydrohalogenation: Enhancing Sorption Capacities through Halogenation to Halofumarate-Based Zr(IV)-Metal-Organic Frameworks, *Chem. Mater.*, 2019, **31**, 8629–8638.

29 D. D. Zhou, P. Chen, C. Wang, S. S. Wang, Y. Du, H. Yan, Z. M. Ye, C. T. He, R. K. Huang, Z. W. Mo, N. Y. Huang and J. P. Zhang, Intermediate-sized molecular sieving of styrene from larger and smaller analogues, *Nat. Mater.*, 2019, **18**, 994–998.

30 S. S. Zheng, B. Li, Y. J. Tang, Q. Li, H. G. Xue and H. Pang, Ultrathin nanosheet-assembled-$Ni_3(OH)_2(PTA)_2(H_2O)_4$ center dot $2H_2O$ hierarchical flowers for high- performance electrocatalysis of glucose oxidation reactions, *Nanoscale*, 2018, **10**, 13270–13276.

31 T. Zheng, Q. Wang, J. Ren, L. Cao, L. Huang, D. Gao, J. Bi and G. Zou, Halogen regulation triggers structural transformation from centrosymmetric to noncentrosymmetric switches in tin phosphate halides Sn_2PO_4X (X = F, Cl), *Inorg. Chem. Front.*, 2022, **9**, 4705–4713.

32 J. L. C. Rowsell and O. M. Yaghi, Effects of functionalization, catenation, and variation of the metal oxide and organic linking units on the low-pressure hydrogen adsorption properties of metal-organic frameworks, *J. Am. Chem. Soc.*, 2006, **128**, 1304–1315.

33 M. B. Kim, K. M. Kim, T. H. Kim, T. U. Yoon, E. J. Kim, J. H. Kim and Y. S. Bae, Highly selective adsorption of SF_6 over N_2 in a bromine-functionalized zirconium-based metal-organic framework, *Chem. Eng. J.*, 2018, **339**, 223–229.

34 H. Wang, J. J. Peng and J. Li, Ligand Functionalization in Metal-Organic Frameworks for Enhanced Carbon Dioxide Adsorption, *Chem. Rec.*, 2016, **16**, 1298–1310.

35 J. Zhang, S. Yao, S. Liu, B. Liu, X. D. Sun, B. Zheng, G. H. Li, Y. Li, Q. S. Huo and Y. L. Liu, Enhancement of Gas Sorption and Separation Performance via Ligand Functionalization within Highly Stable Zirconium-Based Metal-Organic Frameworks, *Cryst. Growth Des.*, 2017, **17**, 2131–2139.

36 W. R. Cheng, S. B. Xi, Z. P. Wu, D. Y. Luan and X. W. Lou, In situ activation of Br-confined Ni-based metal-organic framework hollow prisms toward efficient electrochemical oxygen evolution, *Sci. Adv.*, 2021, **7**, 10.

37 F. Vermoortele, M. Vandichel, B. Van de Voorde, R. Ameloot, M. Waroquier, V. Van Speybroeck and D. E. De Vos, Electronic Effects of Linker Substitution on Lewis Acid Catalysis with Metal-Organic Frameworks, *Angew. Chem., Int. Ed.*, 2012, **51**, 4887–4890.

38 Q. Wu, J. Liang, J. D. Yi, P. C. Shi, Y. B. Huang and R. Cao, Porous nitrogen/halogen dual-doped nanocarbons derived from imidazolium functionalized cationic metal-organic frameworks for highly efficient oxygen reduction reaction, *Sci. China Mater.*, 2019, **62**, 671–680.

39 S. T. Meek, J. J. Perry, S. L. Teich-McGoldrick, J. A. Greathouse and M. D. Allendorf, Complete Series of Monohalogenated Isoreticular Metal-Organic Frameworks: Synthesis and the Importance of Activation Method, *Cryst. Growth Des.*, 2011, **11**, 4309–4312.

40 M. Kalaj, M. R. Momeni, K. C. Bentz, K. S. Barcus, J. M. Palomba, F. Paesani and S. M. Cohen, Halogen bonding in UiO-66 frameworks promotes superior chemical warfare agent simulant degradation, *Chem. Commun.*, 2019, **55**, 3481–3484.

41 K.-L. Zhong and M.-Y. Qian, A novel one-dimensional Co^{II} coordination polymer: catena-poly[[hexaaquacobalt(II)] [[diaquabis(sulfato-kO)cobalt(II)]-μ-4,4′-bipyridine-k^2N:N′] [[triaqua(sulfato-kO)cobalt(II)]-μ-4,4′-bipyridine-k^2N:N′]], *Acta Crystallogr., Sect. C: Cryst. Struct. Commun.*, 2012, **68**, m265–m268.

42 F. L. Li, P. T. Wang, X. Q. Huang, D. J. Young, H. F. Wang, P. Braunstein and J. P. Lang, Large-Scale, Bottom-Up Synthesis of Binary Metal-Organic Framework Nanosheets for Efficient Water Oxidation, *Angew. Chem., Int. Ed.*, 2019, **58**, 7051–7056.

43 S. X. Ju, Y. J. Liu, H. Chen, F. J. Tan, A. H. Yuan, X. Y. Li and G. X. Zhu, In situ Surface Chemistry Engineering of Cobalt-Sulfide Nanosheets for Improved Oxygen Evolution Activity, *ACS Appl. Energy Mater.*, 2019, **2**, 4439–4449.

44 X. D. Wang, J. J. Fang, X. R. Liu, X. Q. Zhang, Q. Q. Lv, Z. X. Xu, X. J. Zhang, W. Zhu and Z. B. Zhuang, Converting biomass into efficient oxygen reduction reaction catalysts for proton exchange membrane fuel cells, *Sci. China Mater.*, 2020, **63**, 524–532.

45 K. Rui, G. Q. Zhao, Y. P. Chen, Y. Lin, Q. Zhou, J. Y. Chen, J. X. Zhu, W. P. Sun, W. Huang and S. X. Dou, Hybrid 2D Dual-Metal-Organic Frameworks for Enhanced Water Oxidation Catalysis, *Adv. Funct. Mater.*, 2018, **28**, 9.

46 R. Zhang, P. A. Russo, A. G. Buzanich, T. Jeon and N. Pinna, Hybrid Organic-Inorganic Transition-Metal Phosphonates as Precursors for Water Oxidation Electrocatalysts, *Adv. Funct. Mater.*, 2017, **27**, 11.